

Entropy-driven nonequilibrium phonon-stimulated electron-phonon coupling in tin dioxide nanorods

G. Mallik, A. Kabiraj¹, D. K. Swain, P. P. Dash, P. Kumari, and S. Rath^{1*}

School of Basic Sciences, Indian Institute of Technology Bhubaneswar, Jatni-752050, Khordha, Odisha, India

 (Received 28 February 2023; revised 7 December 2023; accepted 15 January 2024; published 16 February 2024)

Nonequilibrium (NEQ) phonon fluctuation in a nanosystem has been studied through the statistical assessment of the entropy-production and -consumption events in ultrasmall tin dioxide (SnO₂) nanorods. Size- and shape-dependent alteration in free energy leading to modulation of the probability distribution function of the phonon dynamics has been observed from the x-ray diffraction and Raman scattering characterizations. The Gallavotti-Cohen nonequilibrium fluctuation theorem has been utilized to qualitatively describe the aforementioned behaviors under the influence of a global flux. The observation of entropy consumption and thermodynamically favorable entropy-production events indicates the presence of NEQ fluctuations in the phonon modes. The effective energy scale of fluctuation in driven phonon modes, dissipating energy faster than relaxation time, is quantified on the order of nanojoules. From optical absorption and photoluminescence studies, the observation of the electron-phonon coupled state confirms the interaction of the NEQ phonons with electrons. The strength of the coupling has been estimated from the temperature-independent Barry center shift and found to be enhanced to 5.35. Valence band x-ray photoelectron spectroscopy and Fourier transformed infrared spectroscopy analyses reconcile NEQ phonon mediated alteration of the valence band density of states, activation of silent phonon modes, and superior excitonic transitions, suitable for the new generation of ultrafast quantum device applications.

DOI: [10.1103/PhysRevE.109.024213](https://doi.org/10.1103/PhysRevE.109.024213)

I. INTRODUCTION

Recent advances in phonon behaviors within a nanodimensional volume element have posed potential technological needs [1,2] for quantum coherence [3,4], electrothermal management across nanojunctions [1,5], and molecular motors [6–8]. In common, the quantum confinement effects on the phonon states accomplish quantization in the energy level and broadening in vibrational lines [9]. The theoretical studies by Rowlette and Goodson [1] and Ono [5] shed light on nanoscale heat transport, which is strongly influenced by the scattering dynamics of an excited electron with a transient nonequilibrium (NEQ) phonon (e.g., LO → LA + TA fast decay channel, relaxation time ∼100 fs) compared to the equilibrium optical phonon (LO, relaxation time ∼10 ps) [1,5]. This is due to the readjustment of the phonon occupation number. The deviation of phonon occupation, $n_{\text{ph}}^{\text{NEQ}} = [\exp(\frac{\hbar\omega_{\text{ph}}}{k_{\beta}T_{\text{eff}} + \gamma \hbar\omega_{\text{ph}}}) - 1]^{-1}$ from the equilibrium (Bose-Einstein distribution, $n_{\text{ph}}^{\text{EQ}} = [\exp(\frac{\hbar\omega_{\text{ph}}}{k_{\beta}T}) - 1]^{-1}$) can be explained in terms of the quasieffective temperature, T_{eff} , and the degree of the NEQ parameter, γ [1,5]. The optical excitation in quantum wells, nanowires, or nanorods (NRs) generates electron scattering dominant NEQ phonon states due to the structural anisotropy [10,11]. Here, the NEQ phonon state may be contemplated in the following way: unlike thermal vibration in equilibrium, the lattice vibrations in ultrasmall nanosystems can be envisioned as the large motion

of a very small subset of the vibrational density of states, analogous to a mode of the particle itself having a large amplitude for the atoms. Generally, the fluctuation-dissipation theorem in a system establishes a link between the spontaneous fluctuations at temperature T and its linear response to an external driving force when it is in an equilibrium state. When the system is arbitrarily perturbed far from equilibrium, this fluctuation-dissipation theory fails, as there are appearances of fluctuations in negative and positive amplitudes. According to the Gallavotti and Cohen nonequilibrium fluctuation theorem (GCNEQFT) [12,13], the fluctuation associated with such a system is given by $\lim_{\tau \rightarrow \infty} \frac{P(+S_{\tau})}{P(-S_{\tau})} = e^{\tau S_{\tau}}$, where $P(+S_{\tau})$ and $P(-S_{\tau})$ are the probability fluctuations of amplitude S_{τ} in the rate of entropy production ($+S_{\tau}$) and rate of entropy consumption ($-S_{\tau}$) during the finite time interval (τ), respectively. Notably, in the presence of a time-independent external driving force, if the system achieves a state far away from equilibrium, such a state may be termed as the NEQ steady state. Though the GCNEQFT is widely used in explaining the NEQ fluctuation of vortex states in superconductivity [14], the dragged state of optically trapped colloids [15], resistors [16], jammed states [17], the RNA system [18], and conductivity in quantum systems [19,20], the experimental validation of fluctuating phonon states influencing material characteristics is less explored, in spite of the significant technological implications.

At the same time, metal oxide, viz., tin dioxide (SnO₂), is common in optoelectronics because of its optical transparency and the coexistence of metallic and semiconducting states [21,22]. According to the first-principles level calculations, Chen and Jeng have investigated the concentration (Sn to

*srath@iitbbs.ac.in

O ratio) dependent semiconductor to semimetallic transition phase mediated electron-phonon coupling (EPC) [23]. Such a state exhibits superconducting properties due to the overlapping of the Sn *s*-orbital and O *p*-orbital state functions. Again, the *ab initio* studies predict the softening of the SnO₂ phonon to acoustic modes under pressure [24]. As the nanosystem often exhibits high-pressure states [25,26], a similar effect is inevitable. Nevertheless, several reports mention the fabrication of the SnO₂ nanostructure using both chemical [27,28] and physical deposition techniques [29,30] yielding coarse and irregular shapes with general properties, while the statistical dynamics of the phonon led to the EPC in the SnO₂ nanomaterials are little known due to the lack of fabrication of SnO₂ NRs in the Bohr radius (2.7 nm) regime [27].

This endeavor reveals (i) the phenomenal size-dependent NEQ phonon dynamics in a one-dimensional framework, (ii) the activation of infrared (IR) forbidden phonon modes, and (iii) the temperature-independent EPC state's contribution to the excitonic fine structures of the water-surfactant-alcohol micelles (WSAMs) based grown SnO₂ NRs.

II. EXPERIMENTS

The 10% metal source obtained from 0.05 *M* of (CH₃COO)₄Sn is used in the water-surfactant-alcohol micelles (WSAMs) system for the fabrication of the SnO₂ nanorods. By changing the cetyl-trimethyl-ammonium-bromide (CTAB) concentration from 0.01 to 0.2 *M* at 343 K, we always end up with spherical SnO₂ nanoparticles [31]. An attempt has been made by preparing samples S₁ and S₂ using 0.2 *M* CTAB at temperatures of 130 °C and 160 °C respectively, to understand the effect of temperature on the WSAM based nanostructure formation and growth of the NRs. Notably, 10% butanol is used as a polar additive and cosurfactant in all cases. Since temperature plays an important role in achieving a stable thermodynamical WSAM system, the reagent bottles containing the desired chemicals were kept inside a constant temperature oven for 24 h. Then, the solutions were cleaned thrice with ethanol and double distilled de-ionized (DDI) water using a centrifuge at 9000 rpm for 30 min. The samples were collected on carbon coated copper (Cu) grids and silicon (Si) substrates by the drop casting method for transmission electron microscopy (TEM) and glancing angle x-ray diffraction (GXR) measurements to perceive the morphology and crystallinity of the samples.

The vibrational phonon modes of the samples deposited on the copper substrate were studied using Raman spectroscopy at temperature, 293 K. For Raman measurements, the monochromatic laser of wavelength 457 nm from an argon ion laser source was used as an excitation line with a stabilized steady power supply of 50 mW, focused on the sample area of $\sim 78 \mu\text{m}^2$ through an Olympus microscope attached to the system. The Horiba T64000 triple monochromator attached to a CCD detector was used for Raman signal collection. The spectral resolution of the Raman system is 0.5 cm^{-1} per pixel. Before conducting the measurements, the system was calibrated and optimized with single crystal silicon to 40 000 counts. A highly thermal-conductive copper substrate was used for efficient heat transfer from samples to the sample holder of the Raman instrument to reduce the laser based

heating effect [32]. The substrate was intimately connected to the holder using thermal glue (T670 Chomerics), which may act as a heat sink and reduce the possible heating effect. The small size of the NRs may have added to the heat mitigation by increasing the surface area and roughness of the deposited samples through random distributions (a 1 cm² sample area can accommodate approximately 10¹² nanorods with an area of $\sim 74 \text{ nm}^2$) [33]. The absence of the laser irradiation mediated burning effect has been confirmed through inspections of reproducible microscopic images. The Raman signals were analyzed in a time domain using the inverse fast Fourier transformation (IFFT) technique and the time-binning method. Hence, the instrumental contribution to the fluctuation in Raman modes may be neglected. To correlate the analytical findings of the phonon dynamics of SnO₂ NR samples, the bulk SnO₂ (S₃) purchased from Sigma Aldrich was used for various measurement and comparative studies (see Supplemental Material [34] (Figs. S-1–S-3) for the detailed field effect scanning electron microscope, glancing angle x-ray diffraction (GXR), Raman, and nonequilibrium fluctuation analysis of the bulk sample S₃). The valence band measurements were carried out using the Shimadzu x-ray/ultraviolet photoelectron spectroscopy (XPS/UPS) Kratos Axis Supra setup. The infrared optical properties of the SnO₂ nanorods were studied using a Shimadzu FTIR-8400S Fourier transform infrared (FTIR) spectrometer. The optical properties have been analyzed using the UV-1800 UV-Vis Shimadzu spectrophotometer for absorption and the Horiba Scientific FluoroMax-4 spectrofluorometer for luminescence studies.

A. Formalism of inverse fast Fourier transformation (IFFT)

The experimental Raman data collected in the frequency domain were converted to the time domain for the study of NEQ phonon dynamics. The IFFT is a useful methodology to extract time domain data from experimental frequency domain Raman spectra [41,42] using the expression $I_m(t) = \frac{1}{N} \sum_{n=0}^{N-1} I_n(\omega) e^{2\pi i \frac{m_n t}{N}}$, where $I_m(t)$ is the *m*th component of Raman intensity (amplitude of vibration) in the time domain, $I_n(\omega)$ is the *n*th component of Raman intensity in the frequency domain, m_t is the time resolution, and *N* is the total number of experimental data points.

B. Formulation of the nonequilibrium fluctuation analysis

The phonon dynamics of the ultrasmall SnO₂ NRs shows fluctuations in the Raman mode amplitudes. Using the Gallavotti-Cohen nonequilibrium fluctuation theorem mentioned above, the behaviors of phonon modes are analyzed. When $\tau \rightarrow \infty$, S_τ becomes large, referring to $P(+S_\tau) \gg P(-S_\tau)$ states, and satisfies the classical thermodynamic principle. Here, the τ is larger than any microscopic timescale of the system, and $S_\tau = \frac{\int_t^{t+\tau} S(t') dt'}{\tau}$, with $S(t')$ being the entropy-production rate in the NEQ steady state. Moreover, the global power flux = laser intensity (*I*) \times area of exposure (*A*) that drives the system out of equilibrium refers to a time-independent external driving force. The Raman measurements were conducted in the frequency domain and subsequently converted to the time domain using the IFFT technique. The time-binning methodology was utilized to extract the

probability distribution function with a normalized variable, ω_τ (time period less than the lifetime of the phonon modes). It involves the extraction of the probability distribution of whole data for a given time bin (say, 50 fs). To ensure statistical accuracy and independent sampling, the overlapping bins and the bin's center shift (center of each bin is shifted from the previous one by a time factor of 25 fs, which is larger in comparison to the resolution time ~ 10 fs) methods are used, respectively. Here, the time resolution is the time difference between two consecutive data points. The statistical behaviors of the fluctuations have been analyzed at different time bins from 50 to 200 fs with an overlapping bin of 25 fs. From the experimental data, $\omega_\tau = \frac{S_\tau}{\langle S(t) \rangle} = \frac{1}{\tau} \int_t^{t+\tau} \frac{I_r(t')A}{A \langle I_r \rangle} dt'$ has been extracted, where $I_r(t')$ is the intensity of the time series over a time period (τ) and A is the area of the sample under exposure. To get more insight into the NEQ phonon fluctuation, the average entropies $\langle S(t) \rangle$ of the systems were estimated from the slopes of R versus ω_τ , where $R = \omega_\tau \langle S(t) \rangle = \frac{1}{\tau} \ln \left[\frac{P(+\omega_\tau)}{P(-\omega_\tau)} \right]$. Moreover, the entropy is given by $S(t) = \frac{I(t) \times A}{\epsilon_{\text{eff}}}$, where ϵ_{eff} is an effective energy scale for the dissipation of quasiparticle states (e.g., allowed eigenmodes of lattice vibration) of the system for a very short timescale (i.e., less than the relaxation time period), which is different from that of the equilibrium energy state [14–20]. Further, the degrees of non-Gaussianity of the distributions have been analyzed qualitatively by a shape parameter, kurtosis, $K = \left[\frac{\langle \delta W_\tau^4 \rangle}{\sigma^4} - 3 \right]$ and a metric for nonequilibrium distribution, skewness, $S = \frac{\langle \delta \omega_\tau^3 \rangle}{\sigma^3}$ where $\langle \delta \omega_\tau \rangle = \omega_\tau - \langle \omega_\tau \rangle$ and $\sigma^2 = \langle \delta \omega_\tau^2 \rangle$.

III. RESULTS AND DISCUSSIONS

Figures 1(a) and 1(b) are the TEM micrographs of the samples S_1 and S_2 , revealing the growth of NRs with average diameter and length of 1.7 and 5.2 nm, and 11 and 47 nm, respectively. A histogram of the respective insets shows the distributions of width and length of the NR samples. The sizes of the nanorods are very close to the Bohr exciton radius (2.7 nm), indicating the prevalence of strong confinement effects. Figures 1(c) and 1(d) refer to the high-resolution TEM images depicting crystalline growth along the (1 0 1) plane. Here, the high-resolution micrographs clearly evidenced no physical joining by diffusion between the nanorods. The lattice spacing analysis confirms the growth of the tetragonal phase SnO_2 . Furthermore, the crystal structures are verified using glancing angle x-ray diffraction (GXRD) studies. Figures 1(e) and 1(f) show the GXRD patterns of the samples S_1 and S_2 , respectively. In comparison with the standard JCPDS No. 41–1445 data file, the diffraction patterns corresponding to the crystallographic planes (1 1 0), (1 0 1), (2 1 1), and (1 1 2) refer to the tetragonal phase. The diffraction patterns have been analyzed using the uniform deformation energy density model (UDEDM) [34,43]. According to the UDEDM, the diffraction parameters (e.g., linewidth, diffraction angle, modulus of elasticity) are correlated with free energy by $\beta_{hkl} \cos \theta = \frac{k\lambda}{D} + 4 \sin \theta \left(\frac{2u}{E_{hkl}} \right)^{1/2}$ where β_{hkl} , u , and E_{hkl} are the linewidth, free energy density, and modulus of elasticity for the ($h k l$) planes, respectively. From the slope of the graph, $\beta_{hkl} \cos \theta$ versus $\frac{4 \sin \theta}{E_{hkl}}$, the free energy density

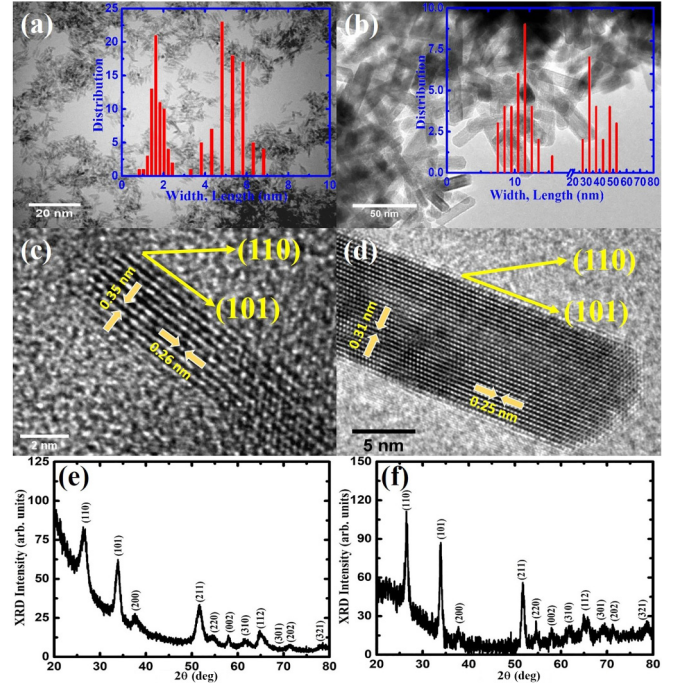


FIG. 1. TEM micrographs of samples, S_1 (a) and S_2 (b). The insets of (a), (b) show the size distribution histograms of the respective samples. (c), (d) are the high-resolution TEM images and (e), (f) are the GXRD patterns of the samples S_1 and S_2 , respectively.

and modulus of elasticity of the samples, S_1 and S_2 , are estimated to be 1537.6 kJ m^{-3} and $1.696 \times 10^{11} \text{ N/m}^2$, and 1081.6 kJ m^{-3} and $1.658 \times 10^{11} \text{ N/m}^2$, respectively (for the details of UDEDM analysis and the $\beta_{hkl} \cos \theta$ versus $\frac{4 \sin \theta}{E_{hkl}}$ plot, see Supplemental Material [34] (Fig. S-4)). Interestingly, the free energy density of smaller NRs is higher than the bigger one with a relatively unaltered elastic modulus.

The free energy density qualitatively discerns the lattice arrangement in a given nanorod based on the vibrational and electronic properties. An extensive study of the lattice dynamics of the NRs systems has been done from the Raman scattering measurements. As shown in Fig. 2, the characteristic vibrational mode (631 cm^{-1}) of a SnO_2 NRs is very distinct in the S_2 sample (shown as a black curve) in contrast with the broadened and cluttered signal in the S_1 sample (shown as a gray curve). The shift and broadening in the Raman mode may be due to the combined action of the strain [44], the phonon confinement effect [45], and fluctuations in phonon density. Even at the near band gap energy excitation, the fluctuations in the phonon modes evidenced intriguing size-dependent dynamics within the timescale of the phonon lifetime (~ 10 ps). Again, considering symmetry, Nitta and Takahashi *et al.* describe the lowering of vibrational symmetry to acoustic modes leading to interactive core and surface oscillation modes guided by the spontaneous breaking of collective oscillation symmetry to quasimassive Nambu-Goldstone modes [46]. Unlike optical absorption or emission properties, where size distribution introduces the broadening in the transition line, the phonon behavior in an ultrasmall NR is analogous to the Gross-Pitaevskii condensate state function, $\Psi = \sqrt{n} e^{i\phi}$, with

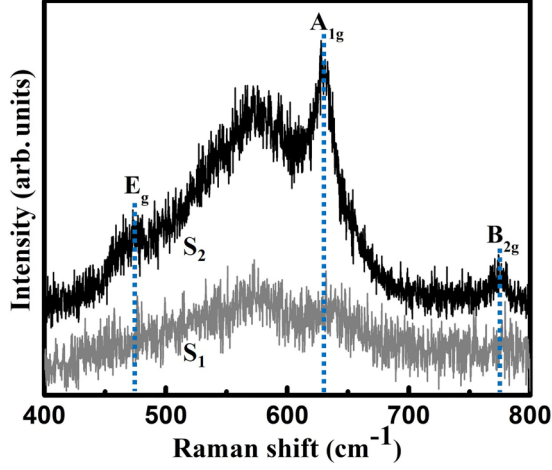


FIG. 2. Raman spectra of S_1 (gray curve) and S_2 (black curve) with blue dotted lines showing the positions of natural Raman vibrations.

$\phi(t, z, \theta, r) = \phi_0 + e^{i(kz+m\theta)} \sum_{n=0}^{\infty} a_n(t) f_{nkm}(r)$, where n is the number density, ϕ is the phase, k is the phonon momentum vector, a_n is the scattering action, and f_{nkm} is the basis for the radial function [47]. Here, the phonon dispersion relation experiences a cylindrical symmetry bounded confinement effect. As a result, phonon scattering follows selection rules like conservation of momentum, radial quantum number, angular quantum number, and longitudinal quantum number, etc. Hence, the aforementioned effects may have influenced the behavior of phonons in our samples. Of late, depending upon the heat exchange among the system \rightleftharpoons surrounding, there have been experimental proofs of signal fluctuations in classical [48], plasma [49], and quantum systems [50]. Therefore, the fluctuating Raman spectra of the SnO_2 NRs were analyzed using the GCNEQFT. Here, the entire range of phonon amplitude versus time plots, ranging from 0 to 20000 fs in the time domain, has been extracted from the frequency range of $400 - 800 \text{ cm}^{-1}$ of the experimental Raman data using the IFFT technique. Figures 3(a) and 3(b) are the normalized amplitude fluctuation versus time plots of samples S_1 and S_2 respectively. The dotted orange line represents the magnitude of mean amplitude fluctuation with reference to zero fluctuation (shown by the white line). The mean amplitude fluctuations of S_1 and S_2 were estimated to be 0.036 and 0.042, respectively, where the amplitudes of negative and positive fluctuations are significantly contributing toward entropy-driven events. Notably, greater magnitude of mean fluctuation refers to the dominance of positive amplitude fluctuation over a negative one, and the driven system is guided by thermodynamic principles. On the contrary, the phonon fluctuations in bulk SnO_2 (see Supplemental Material [34] [Fig. S-3(a)] for the fluctuation analysis of the bulk SnO_2) are only in the positive ordinate, with a mean value of 0.625. This confirms that a driven continuum system is bound to the second law of thermodynamics. Nevertheless, the phonon characteristics in the confined system are very dynamic under the influence of the global flux due to the presence of negative and positive amplitude fluctuations. The GCNEQFT is utilized to explore the phonon

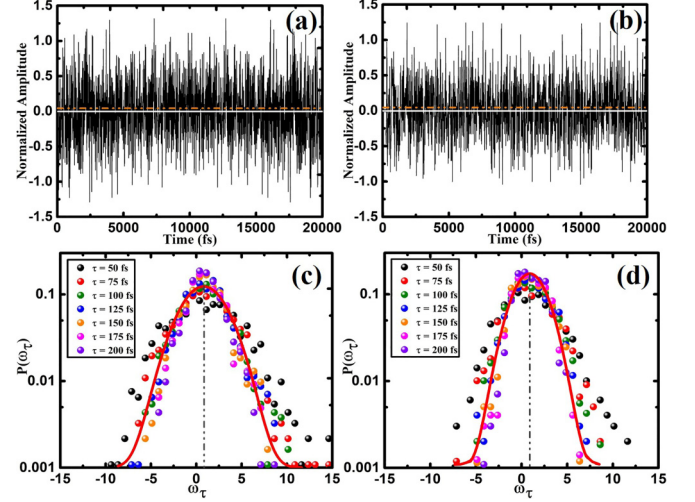


FIG. 3. (a), (c) are the Raman amplitude versus time plot extracted by inverse Fourier transformed Raman data, and the probability distribution amplitude versus normalized variable time series (ω_τ) of sample S_1 . Similarly, for sample S_2 , (b) is the Raman amplitude versus time plot and (d) is the probability distribution.

mediated NEQ behaviors in our samples. From the above fluctuation data, the probability distribution functions versus the normalized variable ω_τ are shown in Figs. 3(c) and 3(d). The distribution plots over bin time periods starting from 50 to 200 fs show the non-Gaussian distributions for $|\omega_\tau| > 6$ and the center of the distribution shifted to 0.821 and 0.905 for S_1 and S_2 , respectively, while for the bulk SnO_2 , the distribution centered at 0.998 (see Supplemental Material [34] [Fig. S-3(b)] for the probability distributions of amplitude fluctuations in bulk SnO_2). The NEQ states are more dominant in the positive ω_τ axis referring to the entropy-production events supporting the second law of thermodynamics, in addition to entropy-consumption values in the negative ω_τ axis. The variation of distribution probability $P(\omega_\tau)$ with ω_τ , in the range $-15 < \omega_\tau < -10$, refers to the degree of entropy consumption averted by thermodynamics; the finite probability in the zone $-10 < \omega_\tau < 0$ refers to the NEQ state under discussion, which shows its repercussions as the asymmetry tail in the entropy-production event ($0 < \omega_\tau < +15$) during the process to regain equilibrium for a longer relaxation time. For a guide to the eye, the solid red curves refer to the Gaussian curve [51], $P(W_\tau) = \frac{1}{\sqrt{2\pi}\Gamma} e^{-\frac{(W_\tau - \langle W_\tau \rangle)^2}{2\Gamma^2}}$, where $\langle W_\tau \rangle$ and Γ are the mean and the standard deviation of W_τ , respectively, and the dotted lines are the centers of the Gaussian distributions. The shift of the center from the origin implies the non-Gaussian nature of the probability distributions of the final state (NEQ state) under the influence of power flux. Hence, the presence of an asymmetric tail in the probability distribution function toward the forward path ($+\omega_\tau$) and a shift in the distribution peak reconciles the dominance of entropy production in association with entropy-consumption events. To get more insight into the NEQ phonon fluctuation, the phenomenon can be restated by a parameter, $R = \frac{1}{\tau} \ln \left[\frac{P(+\omega_\tau)}{P(-\omega_\tau)} \right] = \omega_\tau \langle S(t) \rangle$, where $\langle S(t) \rangle = \frac{\langle I(t) \rangle \times A}{\epsilon_{\text{eff}}}$. The slope of R versus ω_τ yields the average entropy of the system that is

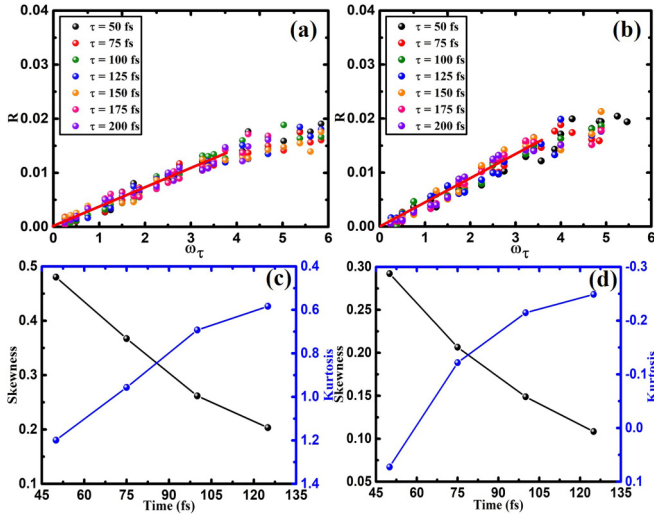


FIG. 4. (a), (b) are the fluctuation relation versus ω_τ plots at different time series of samples S_1 and S_2 , respectively. Skewness (black spheres with black joining lines) and kurtosis (blue spheres with blue joining lines) plots of the samples S_1 (c) and S_2 (d).

independent of the choice of the τ . Figures 4(a) and 4(b) are the R versus ω_τ plots for a range of time bins. The results show a linear variation scale into a single master curve passing through the origin up to $\omega_\tau \sim 3.8$, agreeing with the NEQ fluctuation theorem. From the slope of the linear fitting, the average entropy is estimated to be $(3.65 \pm 0.03) \times 10^{-3} \text{ s}^{-1}$ and $(4.32 \pm 0.03) \times 10^{-3} \text{ s}^{-1}$ for samples S_1 and S_2 respectively. Again, the above analysis sheds light on the effective energy scale, ε_{eff} associated with the dissipation of fluctuating phonon states within a time frame shorter than the relaxation time, which has been estimated as $(0.77 \pm 0.07) \text{ nJ}$ and $(0.75 \pm 0.05) \text{ nJ}$ for S_1 and S_2 , respectively. Bag *et al.* [14] have observed the ε_{eff} on the order of microjoules in the NEQ fluctuation dissipation of the vortex state of a superconductor. The high ε_{eff} values correspond to the high athermal energy dynamics of the global-flux-driven NEQ phonon modes. Based on the observations of the K -shape parameter and skewness from Figs. 4(c) and 4(d), it has been verified that the system is not in an equilibrium state [48].

The NEQ fluctuations enhance phonon generation and absorption events, and make a promising contribution to the advancement of optical devices through electron-phonon coupling. The impact of NEQ phonons in our samples can be assessed through valence band studies, FTIR, and photoluminescence measurements. The UPS measurements have been carried out to understand the valence structure of the samples. Before recording the data, the sample surfaces are cleaned using the argon-ion etching technique. Figures 5(a) and 5(b) show the valence band density of states (DOS) versus binding energy plots of samples S_1 and S_2 , respectively. The valence band DOS for samples consists of five peaks obtained from careful background corrections and fitting. In addition to the prevalent DOS [oxygen $2p$, Sn $5p$ peaking at the binding energy (E_b) 4.40 and 4.66 eV, and 6.01 and 6.19 eV for samples S_1 and S_2], an exciting shoulder-riden DOS corresponding to the Sn $5s$ level has been observed at the binding energy of 2.40 eV in the smaller NRs. This has paved

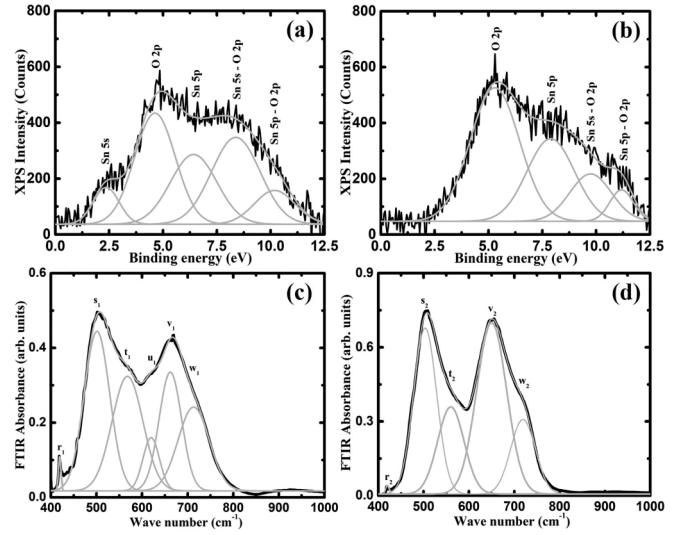


FIG. 5. Valence level XPS spectra (a), (b), and FTIR spectra (c), (d) of samples S_1 and S_2 , respectively. The Gaussian fitting is used for the deconvolution of the experimental results.

the way to establish size-dependent electron-phonon coupled states, as confirmed from the photoluminescence studies (UV excitation). The contribution of the partial $5s$ orbital to the valence can be understood (antibonding Sn $5s - O 2p$ states) from the excess oxygen mediated accommodation of electrons (for the detailed concentration calculations, see Supplemental Material [34] (Fig. S-5)). In addition to this, we have also observed the DOS corresponding to the bonding of Sn $5s - O 2p$ states at the E_b , 8.52 eV, and 8.25 eV for both samples respectively. Furthermore, the deconvoluted peaks at 10.49 and 10.20 eV for samples S_1 and S_2 in the valence band are originated by the autoionization process [52]. For example, as the valence band has been modified due to the influence of the cationic states, upon photoexcitation, the following electronic transition occurs: $4d^{10}(V)^n 5p^0(C) + h\nu \rightarrow [4d^9(V)^n 5p^1(C)]^*$ and the decay follows the emission of the electron through the autoionization process: $[4d^9(V)^n 5p^1(C)]^* \rightarrow [4d^{10}(V)^{n-1} 5p^0(C)] + e^-$, where $5p^0(C)$ and $5p^1(C)$, and (V) are the electronic states of the conduction band and states in the valence band, respectively. The final state obtained after photoexcitation has preserved the dipole selection rule by increasing the photoemission cross section. As a result, we observed the photoemission from the valence band corresponding to the partial Sn $5p - O 2p$ hybridized states. Similar photoemission has been observed by Jimenez *et al.* [52] and Themlin *et al.* [53]. However, there is a shift in peak position to higher energy observed in our samples compared to Refs. [52,53] (bulk SnO_2), which is possibly due to the quantum confinement effect. Therefore, the valence DOS analysis confirms size-dependent alteration and overlapping of conduction band $5s$ - and $5p$ -unoccupied electrons with valence, which leads to the softening of the symmetry of the low-level-lying electronic states.

Figures 5(c) and 5(d) show the Fourier transform infrared (FTIR) spectra of samples S_1 and S_2 , respectively. From the Gaussian peak fitting, the prominent infrared (IR) active bands, $3E_u$ (620 cm^{-1}) and A_{2u} ($713, 719 \text{ cm}^{-1}$),

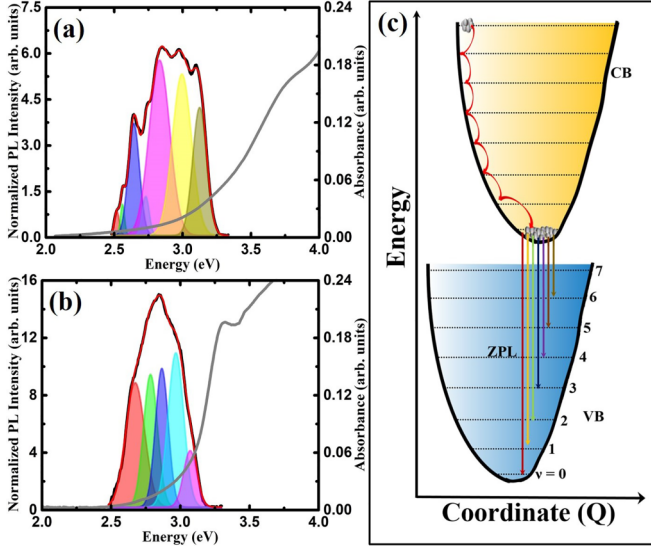


FIG. 6. Optical absorption (gray line) and PL spectra (black line) of samples S₁ (a) and S₂ (b). Using Gaussian function fitting, the peaks of the PL spectra are shown by field colors. (c) Schematic of the electron-phonon interaction in configuration coordinates, relevant to fine structures in our PL studies. The downward arrows represent the contribution of higher-order phonons to the excitonic transitions.

are visible in both the samples. In comparison with theory, the blueshift in IR-active vibrational modes is attributed to the phonon confinement effect [54]. In addition, the IR band appearing at 662 cm^{-1} , and at 650 cm^{-1} in S₁ and S₂ corresponds to the O–Sn–O vibrational modes [55,56]. Remarkably, the IR silent modes (A_{2g} and $2B_u$) are also observed at $419, 420\text{ cm}^{-1}$, and $501, 503\text{ cm}^{-1}$ in S₁ and S₂, respectively. The activation of IR silent modes [57,58] arising from the renormalization of the selection rule and supporting the electron-phonon coupled states can be understood with the following explanation. As the size of the SnO₂ NRs is less than the Bohr exciton diameter, the strong overlapping of the carrier wave function increases the oscillator strength. Upon IR electromagnetic radiation, the quantum confined phonons are strongly coupled with the confined electrons, yielding exciton-phonon coupled states [59], resulting in the activation of IR modes. Again, in our samples, the excess oxygen concentration is probably helping the electron-phonon coupling to soften the selection rule and become IR active, which has been complemented in the valence band and core level (see Supplemental Material [34] (Fig. S-5) for the detailed concentration calculations) XPS analysis. At the same time, the peaks t_1 (568.00 cm^{-1}) and t_2 (559.98 cm^{-1}) may be assigned as the IR activated surface mode [60].

Figures 6(a) and 6(b) show the optical absorption and emission (excitation line $\sim 325\text{ nm}$) of the samples, S₁ and S₂, respectively. The absorption line follows a peak bound characteristic. From the absorption studies, the band gap of the samples has been estimated to be 3.36 eV (S₁) and 3.04 eV (S₂) (see Supplemental Material [34] (Fig. S-6) for the band gap measurement using the Tauc plot method). Notably, in comparison with the bulk, the band gap is observed to be reduced. The correlated many-body (electron-

electron and electron-impurity) interactions [61] dominate the upward and downward shift of the valence band in the presence of excess oxygen [62] and the quantum confinement effect [63], respectively, causing the shrinkage of the band gap. The PL spectra of S₁ exhibit deterministic peak bound fine structures at $2.52, 2.56, 2.64, 2.73, 2.83, 2.99$, and 3.12 eV , whereas S₂ exhibits fine structures at $2.64, 2.77, 2.85, 2.98$, and 3.09 eV , respectively, referring to the transition associated with electron-phonon coupled excitonic states. The above transitions can be explained using the Frank-Condon principle. Considering the quantized harmonic potential (dotted horizontal lines), higher orders of electron-phonon coupled transitions are schematically shown in Fig. 6(c) under the configurational coordinate scheme. Since the “Stokes shift” is correlated with the electron-phonon coupled states [64,65] through $\Delta E = 2\lambda E_{\text{ph}}$, where λ and E_{ph} are electron-phonon coupled constant (Huang-Rhys parameter) and phonon energy ($E_{\text{ph}} - 78\text{ meV}$ [66]) respectively. Moreover, the same shift is strongly dependent on the thermal occupation number of the phonon modes. In order to estimate “ λ ” quantitatively from room temperature optical studies, the temperature-independent average energy of the optical transition (absorption and/or emission) can be determined from the “barycenter” [64] $E_{\text{bc}} = \frac{\int W(E)E dE}{\int W(E) dE}$, where $W(E)$ is the optical transition moment and E is the transition energy such that the optical absorbance $\alpha(E) \sim EW(E)$ and the emission intensity $\rho(E) \sim E^3W(E)$ [67]. Now the difference in barycenter becomes $\Delta E_{\text{bc}} = E_{\text{bc}}^{\text{abs}} - E_{\text{bc}}^{\text{em}} = 2\lambda E_{\text{ph}}$. Using the above expression, λ has been estimated as 5.35 and 3.55 for S₁ and S₂, respectively, indicating strong electron-phonon coupling in S₁ as compared to S₂. Similar λ has been observed in other SnO₂ systems [68,69].

IV. CONCLUSION

We have demonstrated a phenomenal size-dependent nonequilibrium phonon fluctuation mediated electron-phonon coupling from WASAM based, grown SnO₂ nanorods. As observed from the GXR analysis, the free energy density of the smaller NRs (1537.6 kJ m^{-3}) is observed to be larger than the bigger one (1081.6 kJ m^{-3}). In the framework of nonequilibrium fluctuation, the size-dependent amplitude fluctuations of the driven phonon states, revealing the entropy-production and -consumption events, have been compared. The effective energy scale associated with the dissipation of fluctuating phonon states within a time frame shorter than the relaxation time is found to be on the order of nanojoules. The photoluminescence studies corroborate the nonequilibrium phonon states associated with enhancement of the electron-phonon coupling (coupling parameter increase to 5.35) for the strongly confined phonon states. This unfolds the statistical behavior of phonons in a nonequilibrium steady state suitable for electrothermal management and fast quantum device applications.

ACKNOWLEDGMENTS

The authors acknowledge the financial support received from Nano-mission, Department of Science and Technology India, under Scheme No. SR/NM/NS-68/2016 (G) and the Science and Engineering Research Board, DST India under Scheme No. CRG/2020/003163.

- [1] J. A. Rowlette and K. E. Goodson, Fully coupled nonequilibrium electron-phonon transport in nanometer-scale silicon FETs, *IEEE Trans. Electron Devices* **55**, 220 (2008).
- [2] F. Caruso, Nonequilibrium lattice dynamics in monolayer MoS₂, *J. Phys. Chem. Lett.* **12**, 1734 (2021).
- [3] A. Belenchia, L. Mancino, G. T. Landi, and M. Paternostro, Entropy production in continuously measured Gaussian quantum systems, *npj Quantum Inf.* **6**, 97 (2020).
- [4] J. P. Santos, L. C. Céleri, G. T. Landi, and M. Paternostro, The role of quantum coherence in non-equilibrium entropy production, *npj Quantum Inf.* **5**, 23 (2019).
- [5] S. Ono, Nonequilibrium phonon dynamics beyond the quasiequilibrium approach, *Phys. Rev. B* **96**, 024301 (2017).
- [6] C. Bustamante, J. Liphardt, and F. Ritort, The nonequilibrium thermodynamics of small systems, *Phys. Today* **58**, 43 (2005).
- [7] V. G. Almendro-Vedia, P. Natale, M. Mell, S. Bonneau, F. Monroy, F. Joubert, and I. López-Montero, Nonequilibrium fluctuations of lipid membranes by the rotating motor protein F1FO-ATP synthase, *Proc. Natl. Acad. Sci. USA* **114**, 11291 (2017).
- [8] A. Gnoli, A. Sarracino, A. Puglisi, and A. Petri, Nonequilibrium fluctuations in a frictional granular motor: Experiments and kinetic theory, *Phys. Rev. E* **87**, 052209 (2013).
- [9] F. W. Wise, Lead salt quantum dots: The limit of strong quantum confinement, *Acc. Chem. Res.* **33**, 773 (2000).
- [10] A. Krishnamoorthy, M. F. Lin, X. Zhang, C. Weninger, R. Ma, A. Britz, C. S. Tiwary, V. Kochat, A. Apte, J. Yang, S. Park, R. Li, X. Shen, X. Wang, R. Kalia, A. Nakano, F. Shimojo, D. Fritz, U. Bergmann, P. Ajayan, and P. Vashishta, Optical control of non-equilibrium phonon dynamics, *Nano Lett.* **19**, 4981 (2019).
- [11] L. Waldecker, R. Bertoni, R. Ernstorfer, and J. Vorberger, Electron-phonon coupling and energy flow in a simple metal beyond the two-temperature approximation, *Phys. Rev. X* **6**, 021003 (2016).
- [12] G. Gallavotti and E. G. D. Cohen, Dynamical ensembles in stationary states, *J. Stat. Phys.* **80**, 931 (1995).
- [13] G. Gallavotti and E. G. D. Cohen, Dynamical ensembles in nonequilibrium statistical mechanics, *Phys. Rev. Lett.* **74**, 2694 (1995).
- [14] B. Bag, G. Shaw, S. S. Banerjee, S. Majumdar, A. K. Sood, and A. K. Grover, Negative velocity fluctuations and non-equilibrium fluctuation relation for a driven high critical current vortex state, *Sci. Rep.* **7**, 5531 (2017).
- [15] G. M. Wang, E. M. Sevick, E. Mittag, D. J. Searles, and D. J. Evans, Experimental demonstration of violations of the second law of thermodynamics for small systems and short time scales, *Phys. Rev. Lett.* **89**, 050601 (2002).
- [16] N. Garnier and S. Ciliberto, Nonequilibrium fluctuations in a resistor, *Phys. Rev. E* **71**, 060101(R) (2005).
- [17] S. Majumdar and A. K. Sood, Nonequilibrium fluctuation relation for sheared micellar gel in a jammed state, *Phys. Rev. Lett.* **101**, 078301 (2008).
- [18] D. Collin, F. Ritort, C. Jarzynski, S. B. Smith, I. Tinoco, and C. Bustamante, Verification of the Crooks fluctuation theorem and recovery of RNA folding free energies, *Nature (London)* **437**, 231 (2005).
- [19] J. Gieseler, R. Quidant, C. Dellago, and L. Novotny, Dynamic relaxation of a levitated nanoparticle from a non-equilibrium steady state, *Nat. Nanotechnol.* **9**, 358 (2014).
- [20] J. Liphardt, S. Dumont, S. B. Smith, I. Tinoco, and C. Bustamante, Equilibrium information from nonequilibrium measurements in an experimental test of Jarzynski's equality, *Science* **296**, 1832 (2002).
- [21] M. M. Bagheri Mohagheghi, S. Tabatabai Yazdi, and M. Mousavi, Transport, structural and optical properties of SnO₂ transparent semiconductor thin films alloyed with chromium: Carrier type conversion, *J. Mater. Sci. Mater. Electron.* **28**, 13328 (2017).
- [22] I. M. Costa, E. P. Bernardo, B. S. Marangoni, E. R. Leite, and A. J. Chiquito, Metal to insulator transition in Sb doped SnO₂ monocrystalline nanowires thin films, *J. Appl. Phys.* **120**, 225109 (2016).
- [23] P. J. Chen and H. T. Jeng, Phase diagram of the layered oxide SnO: GW and electron-phonon studies, *Sci. Rep.* **5**, 16359 (2015).
- [24] K. Parlinski and Y. Kawazoe, *Ab initio* study of phonons in the rutile structure of SnO₂ under pressure, *Eur. Phys. J. B* **13**, 679 (2000).
- [25] D. Machon, V. Pischedda, S. Le Floch, and A. San-Miguel, Perspective: High pressure transformations in nanomaterials and opportunities in material design, *J. Appl. Phys.* **124**, 160902 (2018).
- [26] G. Kaptay, The extension of the phase rule to nano-systems and on the quaternary point in one-component nano phase diagrams, *J. Nanosci. Nanotechnol.* **10**, 8164 (2010).
- [27] S. Wu, H. Cao, S. Yin, X. Liu, and X. Zhang, Amino acid-assisted hydrothermal synthesis and photocatalysis of SnO₂ nanocrystals, *J. Phys. Chem. C* **113**, 17893 (2009).
- [28] Z. Xu, Y. Jiang, Z. Li, C. Chen, X. Kong, Y. Chen, G. Zhou, J. M. Liu, K. Kempa, and J. Gao, Rapid microwave-assisted synthesis of SnO₂ quantum dots for efficient planar Perovskite solar cells, *ACS Appl. Energy Mater.* **4**, 1887 (2021).
- [29] J. Y. Bae, J. Park, H. Y. Kim, H. S. Kim, and J. S. Park, Facile route to the controlled synthesis of tetragonal and orthorhombic SnO₂ films by mist chemical vapor deposition, *ACS Appl. Mater. Interfaces* **7**, 12074 (2015).
- [30] L. Zhang, S. Ge, Y. Zuo, B. Zhang, and L. Xi, Influence of oxygen flow rate on the morphology and magnetism of SnO₂ nanostructures, *J. Phys. Chem. C* **114**, 7541 (2010).
- [31] S. Rath, S. Nozaki, H. Ono, K. Uchida, and S. Khajima, Growth and optical properties of SnO₂ ultra-small nanorods by the novel micelle techniques, *Mater. Res. Soc. Symp. Proc.* **1087**, 17 (2008).
- [32] S. K. Mohanty, Y. Y. Chen, P. H. Yeh, and R. H. Horng, Thermal management of GaN-on-Si high electron mobility transistor by copper filled micro-trench structure, *Sci. Rep.* **9**, 19691 (2019).
- [33] H. Peng, G. Ding, H. Hu, and W. Jiang, Effect of nanoparticle size on nucleate pool boiling heat transfer of refrigerant/oil mixture with nanoparticles, *Int. J. Heat Mass Transfer* **54**, 1839 (2011).
- [34] See Supplemental Material at <http://link.aps.org/supplemental/10.1103/PhysRevE.109.024213> for the detailed SEM, GXR, Raman, and nonequilibrium analysis of bulk SnO₂. The GXR investigation, composition analysis from core-level XPS data, and band gap estimation from optical absorption spectra of

- SnO₂ NRs with relevant images are also available in the Supplemental Material. It also contains Refs. [35–40].
- [35] R. Kubo, The fluctuation-dissipation theorem, *Rep. Prog. Phys.* **29**, 255 (1966).
- [36] E. Z. Gusakov and A. Y. Popov, Non-linear theory of fluctuation reflectometry, *Plasma Phys. Controll. Fusion* **44**, 2327 (2002).
- [37] K. Manikandan, S. Dhanuskodi, A. R. Thomas, N. Maheswari, G. Muralidharan, and D. Sastikumar, Size-strain distribution analysis of SnO₂ nanoparticles and their multifunctional applications as fiber optic gas sensors, supercapacitors and optical limiters, *RSC Adv.* **6**, 90559 (2016).
- [38] S. Gürakar and T. Serin, Comprehensive structural analysis and electrical properties of (Cu, Al and In)-doped SnO₂ thin films, *Mater. Sci. Eng. B* **251**, 114445 (2019).
- [39] J. Nayak, S. Varma, D. Paramanik, and S. N. Sahu, Composition and optical characteristics of electrochemically-synthesized GaAs nanocrystals, *Int. J. Nanosci.* **3**, 281 (2004).
- [40] S. H. Skjærvø, E. T. Wefring, S. K. Nesdal, N. H. Gaukås, G. H. Olsen, J. Glaum, T. Tybell, and S. M. Selbach, Interstitial oxygen as a source of *p*-type conductivity in hexagonal manganites, *Nat. Commun.* **7**, 13745 (2016).
- [41] C. K. Kim, K. Lee, and Y. S. Cho, Adaptive beamforming algorithm for OFDM systems with antenna arrays, *IEEE Trans. Consum. Electron.* **46**, 1052 (2000).
- [42] B. Wang, W. Chu, and O. V. Prezhdo, Interpolating nonadiabatic molecular dynamics Hamiltonian with inverse fast Fourier transform, *J. Phys. Chem. Lett.* **13**, 331 (2022).
- [43] P. Muhammed Shafi and A. Chandra Bose, Impact of crystalline defects and size on x-ray line broadening: A phenomenological approach for tetragonal SnO₂ nanocrystals, *AIP Adv.* **5**, 057137 (2015).
- [44] Z. V. Popović, Z. Dohčević-Mitrović, M. Šćepanović, M. Grujić-Brojčin, and S. Aškračić, Raman scattering on nanomaterials and nanostructures, *Ann. Phys. (Leipzig)* **523**, 62 (2011).
- [45] R. Wang, G. Zhou, Y. Liu, S. Pan, H. Zhang, D. Yu, and Z. Zhang, Raman spectral study of silicon nanowires: High-order scattering and phonon confinement effects, *Phys. Rev. B* **61**, 16827 (2000).
- [46] M. Nitta and D. A. Takahashi, Quasi-Nambu-Goldstone modes in nonrelativistic systems, *Phys. Rev. D* **91**, 025018 (2015).
- [47] S. Eckel and T. Jacobson, Phonon redshift and Hubble friction in an expanding BEC, *SciPost Phys.* **10**, 064 (2021).
- [48] N. Kumar, S. Ramaswamy, and A. K. Sood, Symmetry properties of the large-deviation function of the velocity of a self-propelled polar particle, *Phys. Rev. Lett.* **106**, 118001 (2011).
- [49] C.-S. Wong, J. Goree, Z. Haralson, and B. Liu, Strongly coupled plasmas obey the fluctuation theorem for entropy production, *Nat. Phys.* **14**, 21 (2018).
- [50] D. J. Sivananda, N. Roy, P. C. Mahato, and S. S. Banerjee, Exploring the non-equilibrium fluctuation relation for quantum mechanical tunneling of electrons across a modulating barrier, *Phys. Rev. Res.* **2**, 043237 (2020).
- [51] S. Majumdar and A. K. Sood, Statistical properties of entropy-consuming fluctuations in jammed states of laponite suspensions: Fluctuation relations and generalized Gumbel distribution, *Phys. Rev. E* **85**, 041404 (2012).
- [52] V. M. Jimenez, G. Lassaletta, A. Fernandez, J. P. Espinos, F. Yubero, A. R. Gonzalez-Elipe, L. Soriano, J. M. Sanz, and D. A. Papaconstantopoulos, Resonant photoemission characterization of SnO, *Phys. Rev. B* **60**, 11171 (1999).
- [53] J. M. Themlin, R. Sporcken, J. Darville, R. Caudano, J. M. Gilles, and R. L. Johnson, Resonant-photoemission study of SnO₂: Cationic origin of the defect band-gap states, *Phys. Rev. B* **42**, 11914 (1990).
- [54] A. H. Shah, E. Manikandan, M. Basheer Ahamed, D. Ahmad Mir, and S. Ahmad Mir, Antibacterial and blue shift investigations in sol-gel synthesized Cr_xZn_{1-x}O nanostructures, *J. Lumin.* **145**, 944 (2014).
- [55] D. Amalric-Popescu and F. Bozon-Verduraz, Infrared studies on SnO₂ and Pd/SnO₂, *Catal. Today* **70**, 139 (2001).
- [56] W. Matysiak, T. Tański, W. Smok, and O. Polishchuk, Synthesis of hybrid amorphous/crystalline SnO₂ 1D nanostructures: Investigation of morphology, structure and optical properties, *Sci. Rep.* **10**, 14802 (2020).
- [57] A. Priya, E. Sinha, and S. K. Rout, Structural, optical and microwave dielectric properties of Ba_{1-x}Sr_xWO₄ ceramics prepared by solid state reaction route, *Solid State Sci.* **20**, 40 (2013).
- [58] R. L. Frost, L. Duong, and M. Weier, Raman microscopy of selected tungstate minerals, *Spectrochim. Acta, Part A* **60**, 1853 (2004).
- [59] R. Pandya, R. Y. S. Chen, A. Cheminal, M. Dufour, J. M. Richter, T. H. Thomas, S. Ahmed, A. Sadhanala, E. P. Booker, G. Divitini, F. Deschler, N. C. Greenham, S. Ithurria, and A. Rao, Exciton-phonon interactions govern charge-transfer-state dynamics in CdSe/CdTe two-dimensional colloidal heterostructures, *J. Am. Chem. Soc.* **140**, 14097 (2018).
- [60] S. Loridant, Determination of the maximum vanadium oxide coverage on SnO₂ with a high surface area by Raman spectroscopy, *J. Phys. Chem. B* **106**, 13273 (2002).
- [61] K. F. Berggren and B. E. Sernelius, Band-gap narrowing in heavily doped many-valley semiconductors, *Phys. Rev. B* **24**, 1971 (1981).
- [62] A. Yildiz, E. Ozturk, A. Atilgan, M. Sbeta, A. Atli, and T. Serin, An understanding of the band gap shrinkage in Sn-doped ZnO for dye-sensitized solar cells, *J. Electron. Mater.* **46**, 6739 (2017).
- [63] L. Shi and H. Lin, Facile fabrication and optical property of hollow SnO₂ spheres and their application in water treatment, *Langmuir* **26**, 18718 (2010).
- [64] M. De Jong, L. Seijo, A. Meijerink, and F. T. Rabouw, Resolving the ambiguity in the relation between Stokes shift and Huang-Rhys parameter, *Phys. Chem. Chem. Phys.* **17**, 16959 (2015).
- [65] A. P. Voitovich, V. S. Kalinov, A. V. Mudryi, V. N. Pavlovskii, L. P. Runets, and I. E. Svitsiankou, Zero-phonon lines and electron-phonon interaction characteristics of near-surface layer radiation color centers in lithium fluoride, *J. Lumin.* **172**, 147 (2016).
- [66] E. Burkel, J. Peisl, and B. Dorner, Observation of inelastic x-ray scattering from phonons, *EPL* **3**, 957 (1987).
- [67] E. Ejder, Methods of representing emission, excitation, and photoconductivity spectra, *J. Opt. Soc. Am.* **59**, 223 (1969).

- [68] T. Arai and S. Adachi, IR emission band and multiple-peak structure in photoluminescence spectra of SnO₂: Mn, *ECS J. Solid State Sci. Technol.* **2**, R172 (2013).
- [69] T. Arai and S. Adachi, Simple wet chemical synthesis and photoluminescence characterization of SnO₂: Eu³⁺ reddish-orange phosphor, *J. Lumin.* **153**, 46 (2014).